Applied Physics Letters

Aberration characterization of x-ray optics using multi-modal ptychography and a partially coherent source

Cite as: Appl. Phys. Lett. **118**, 104104 (2021); https://doi.org/10.1063/5.0041341
Submitted: 22 December 2020 • Accepted: 19 February 2021 • Published Online: 10 March 2021

Thomas E. J. Moxham, David Laundy, Vishal Dhamgaye, et al.

View Online Export Citation CrossMark

ARTICLES YOU MAY BE INTERESTED IN

Upscaling of multi-beam x-ray ptychography for efficient x-ray microscopy with high resolution and large field of view
Applied Physics Letters **118**, 171102 (2021); https://doi.org/10.1063/5.0045571

AI-enabled high-resolution scanning coherent diffraction imaging
Applied Physics Letters **117**, 044103 (2020); https://doi.org/10.1063/5.0013065

X-ray ptychography on low-dimensional hard-condensed matter materials
Applied Physics Reviews **6**, 011306 (2019); https://doi.org/10.1063/1.5045131

Lock-in Amplifiers up to 600 MHz
Zurich Instruments
Watch

© 2021 Author(s).

Applied Physics Letters ARTICLE scitation.org/journal/apl

Aberration characterization of x-ray optics using multi-modal ptychography and a partially coherent source

Cite as: Appl. Phys. Lett. **118**, 104104 (2021); doi: 10.1063/5.0041341
Submitted: 22 December 2020 · Accepted: 19 February 2021 ·
Published Online: 10 March 2021

View Online Export Citation CrossMark

Thomas E. J. Moxham,[1,2,a)] David Laundy,[2] Vishal Dhamgaye,[2,3] Oliver J. L. Fox,[2] Kawal Sawhney,[2] and Alexander M. Korsunsky[1]

AFFILIATIONS

[1]Department of Engineering Science, University of Oxford, Parks Road, Oxford OX1 3PJ, United Kingdom
[2]Diamond Light Source, Harwell Science and Innovation Campus, Didcot OX11 0DE, United Kingdom
[3]Synchrotron Utilisation Section, Raja Ramanna Centre for Advanced Technology, Indore 452 013, India

[a)]Author to whom correspondence should be addressed: thomas.moxham@eng.ox.ac.uk

ABSTRACT

Ptychography is a scanning coherent diffraction imaging technique that provides high-resolution imaging and complete spatial information of the complex probe and object transmission function. The wavefront error caused by aberrated optics has previously been recovered using ptychography when a highly coherent source is used, but has not been demonstrated with partial coherence due to the multi-modal probe required. Here, we demonstrate that partial coherence can be accounted for in ptychographic reconstructions using the multi-modal approach and assuming that decoherence arises from either the probe or the object. This equivalence recovers coherent (or single state) reconstructions of both the probe and the object even in the presence of partial coherence. We demonstrate this experimentally by using hard x-ray ptychography with a partially coherent source to image a Siemens star test object and to also recover the wavefront error from an aberrated beryllium compound refractive lens. The source properties and resolving capabilities are analyzed, and the wavefront error results are compared with another at-wavelength metrology technique. Our work demonstrates the capability of ptychography to provide high-resolution imaging and optics characterization even in the presence of partial coherence.

© 2021 Author(s). All article content, except where otherwise noted, is licensed under a Creative Commons Attribution (CC BY) license (http://creativecommons.org/licenses/by/4.0/). https://doi.org/10.1063/5.0041341

Advancements in low emittance synchrotron sources and x-ray free electron lasers (XFELs) have led to the development of a range of coherent diffraction imaging (CDI) techniques capable of providing resolutions beyond that of the diffraction limit of traditional optics.[1] Ptychography is one such technique that is able to recover the complex illumination and transmission functions of extended objects by solving the phase problem using diffraction patterns at different overlapping positions.[2,3] It has been employed extensively with visible light, x-rays, and electrons for various microscopic[4–6] and tomographic[7–9] studies, primarily due to its unmatched resolving capabilities and high chemical sensitivity. Its ability to accurately recover the illuminating probe has led to its development as an at-wavelength metrology technique,[10] and the recovered electric field of the probe can be propagated to any plane along the optical axis to measure the focal size and object offset position,[11] optimally align optical elements,[12] and characterize wavefront errors introduced by optical aberrations.[13]

As a wavefront characterization technique, ptychography has been demonstrated with highly transverse-coherent, insertion device beamlines at multiple synchrotron[14,15] and XFEL[16,17] facilities. The small source size and high photon flux mean that the beam can easily be made coherent by filtering without detriment to the overall flux. Inclusion of partial transverse coherence in phase retrieval algorithms initially used Gaussian distributions to model synchrotron sources and required *a priori* knowledge of the source spatial distribution.[18] The most recent and successful algorithmic improvements incorporate a multi-modal approach, which instead decomposes the object and probe functions as a sum of mutually incoherent modes.[19] Multi-modal ptychography had been previously demonstrated to characterize a range of x-ray focusing optics including Kirkpatrick–Baez mirror,[20] multi-layer Laue lens,[21] and Fresnel zone plate.[11] In these studies, the optics focal size and position were characterized using the reconstructed multi-modal probe intensity; however, detailed analysis

of the wavefront error introduced by optical aberrations requires a single coherent probe mode.[13]

The motivation for this study came from the demonstration of multi-modal probe correcting decoherence effects arising from the object;[22,23] in this Letter, we propose that the converse is also true, i.e., that decoherence effects from the probe can be accounted for by considering a multi-modal object. The ptychography experiment was performed on a bending magnet beamline that featured a large source and low transverse coherence, and a beryllium compound refractive lens (CRL) was used to produce a focused probe on a Siemens star test object. Two multi-modal reconstruction[19] approaches were used in which the object and the probe were each considered the source of decoherence. This produced a coherent probe (and a multi-modal object) and a coherent object (and a multi-modal probe). The coherent probe was then back propagated to the Beryllium CRL exit plane, where the wavefront error was computed and compared with previously known data.[24] Finally, we quantify the obtained object resolution using Fourier ring correlation and briefly comment on the coherence properties of the source.

With far-field ptychography, an object $O(\boldsymbol{r})$ is illuminated with a probe $P(\boldsymbol{r})$ and scanned transversely in order to produce a set of diffraction patterns $I_j(\boldsymbol{r})$ at each position $\boldsymbol{r}_j$. If the object is sufficiently thin, propagation effects within the object can be ignored and the exit wave $\psi_j(\boldsymbol{q})$ is simply given as the product of the probe and object functions. From the Fraunhofer approximation, the far-field intensity patterns are proportional to the modulus squared Fourier transform of the exit wave and given by

$$I_j(\boldsymbol{q}) = |\mathcal{F}\{\psi_j(\boldsymbol{r})\}|^2 = |\mathcal{F}\{P(\boldsymbol{r})O(\boldsymbol{r}+\boldsymbol{r}_j)\}|^2, \quad (1)$$

where $\boldsymbol{r}$ is the two-dimensional real space position coordinate, $O(\boldsymbol{r})$ is the complex object function, $P(\boldsymbol{r})$ is the complex illumination function, and $\mathcal{F}$ denotes the Fourier transform with the corresponding reciprocal space coordinate $\boldsymbol{q}$. The aim of the phase retrieval algorithm is to find values for $P(\boldsymbol{r})$ and $O(\boldsymbol{r})$, which agree with the experimentally measured intensities $I_j(\boldsymbol{q})$. A popular class of methods are iterative phase retrieval algorithms,[2,3] which replace the exit wave modulus at each position with the corresponding inverse Fourier transform of the measured diffraction pattern, but allow the phase to vary. Depending on the algorithm used, the probe and object functions are then updated by dividing out a weighted average object and probe function from the updated exit wave, respectively.

Generally, the experimentally measured diffraction patterns are subject to degradation due to decoherence effects arising from partial transverse[11] and longitudinal[25] coherence, sample dynamics,[23] and detector point spread.[19] While each effect may be the cause of an individual complex interaction, they all share the same commonality of reducing the so-called fringe or speckle visibility in the diffracted intensities[19] and can cause the phase retrieval algorithm to fail. Partial transverse coherence has previously been accommodated[22,23] by considering the propagation of the mutual optical intensity of the probe and the density function of the object as a sum of mutually incoherent, orthogonal modes. This reduces the minimization problem of Eq. (1) and only requires the incoherent sum of modal contributions to match the measured diffraction patterns, such that

$$I_j(\boldsymbol{q}) = \sum_{n=1}^{N}\sum_{m=1}^{M}\eta_n\mu_m|\mathcal{F}\{P_n(\boldsymbol{r})O_m(\boldsymbol{r}+\boldsymbol{r}_j)\}|^2, \quad (2)$$

where $P_n(\boldsymbol{r})$ and $O_m(\boldsymbol{r})$ are the modal probe and object functions and η_n and μ_n are the corresponding modal weights. The symmetry between the probe and object functions of Eq. (2) demonstrates that partial coherence effects can be accounted for by either function. This has previously been demonstrated for continuous "fly" scanning ptychography[22] and a vibrating sample,[23] where in both cases, the primary element of interest was the retrieved object function, rather than the probe function as we wish to consider.

Experiments were performed on the B16 Test beamline at the Diamond Light Source, a bending dipole magnet beamline that provided an unfocused, monochromatic beam.[26] In order to maximize the available flux, at no point were slits used to filter the transverse coherence, this provided an approximate flux of 1×10^8 photons/s at the object position. A double-crystal Si(111) monochromator with a bandpass of $\Delta E/E \sim 10^{-4}$ was used to select an x-ray energy of 12 keV and maximize longitudinal coherence. The beam was focused using a Beryllium CRL with a geometric aperture of 1 mm and 98 individual lenses each with a radius of curvature of 200 μm, giving a focal length of 432 mm and an effective aperture of 394 μm at 12 keV. For the test object, a 3 μm thick gold Siemens star on a silicon nitride substrate was positioned slightly downstream of the focal plane on high-precision Attocube piezoelectric translational stages. The Siemens star had a diameter of 400 μm and featured an inner spoke separation of 1 μm as the smallest feature size. A single-photon counting, third-generation Merlin Medipix detector with a pixel size of 55×55 μm^2 and a pixel field of view of 512×512 was positioned 8.4 m downstream of the object. A schematic of the ptychography experimental setup on the B16 Test beamline is shown in Fig. 1.

Ptychography scans were performed by translating the object through the beam and acquiring diffraction patterns at each position, which were done in a spiral manner to reduce raster artifacts.[3] Due to the high level of decoherence from the source, it was thought the

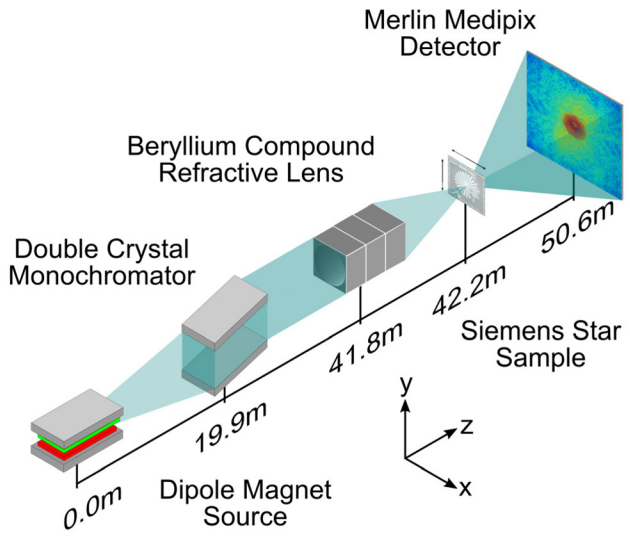

FIG. 1. Schematic of the experimental setup and distances (not to scale) used for ptychography on the B16 Test beamline at the Diamond Light Source. The x-ray beam was generated using a bending dipole magnet source, and the energy was selected using a Si(111) double-crystal monochromator. The beam was then focused by a beryllium compound refractive lens, and the object scanned transversely to the beam close to the focus. Diffraction patterns were collected downstream using a single-photon counting detector.

© Author(s) 2021

typical sampling condition[27] would not be valid, and thus, steps were taken to maximize the sampling. As has been shown previously,[28] denser sampling in the real space can compensate for sparse sampling in reciprocal space and vice versa, and we, therefore, positioned the detector as far downstream of the object as possible and also scanned with a small beam close to the focus. A scan was performed over an area of $32 \times 32\ \mu m^2$ with a step size of 500 nm and an individual exposure time of 0.5 s, which generated 4099 diffraction patterns for ptychographic reconstruction. Initial reconstructions were processed during the experimental session using the ptypy[29] framework and the difference map[30] algorithm with a multi-modal probe. In post-processing, it was realized that to model the probe sufficiently, many more probe modes were required than are typically used and the ptypy implementation was not suitable for efficient reconstruction due to the large memory requirements.

A more suitable method was found with an implementation of the regularized ptychographic iterative engine[31] (rPIE), which involves a sequential update of the probe and object functions by looping through all diffraction patterns. This was extended to use multiple modes using the same minimization procedure outlined in the supplementary material of Ref. 19. A fast GPU implementation of the algorithm was employed using the CuPy[32] python module and an Nvidia Tesla P100. The diffraction patterns were cropped to a region of interest around the optical axis measuring 256×256 pixels, which included only statistically relevant counts. Dead and hot detector pixels were also disregarded from the reconstruction by generating a detector mask based on the integrated diffraction data stack.

Two separate reconstructions were run, one considering the probe and the other, the object as the source of decoherence. For the first reconstruction, a single object was used and probe modes were included up until the relative modal power in the final mode was negligible. This occurred at around 100 modes. In the second reconstruction, a single probe was used and 100 object modes were included for consistency. Both reconstructions started with a flat object function and the simulated probe of an ideal CRL lens, and modes were then included as random permutations of the initial probe and object functions. The rPIE algorithm was run for 750 iterations after which both reconstructions converged to suitable minima. From the summed intensity contributions of the individual modes of the multi-modal probe, the full width half maximum (FWHM) at the object was found to be around $1.65\ \mu m$ (h) $\times$ $0.75\ \mu m$ (v), which is shown in Fig. 2(a). For the experimental geometry outlined, an effective pixel size of 61.6 nm was achieved, and the reconstructed complex object and probe functions for the multi-modal probe and multi-modal object configurations are shown in Figs. 3(a) and 3(b), respectively. The dominant probe (after orthogonalization) and object modes for each respective reconstruction are also included in the supplementary material for completeness.

It was found from the relative power spectrum of the multimodal probe[11] shown in Fig. 2(b) that the normalized degree of coherence (or percentage of transverse coherent flux) was around 2.0%. This agrees well with the theoretically predicted value of 2.02%, calculated using the coherence length[33] and the effective aperture of the optic. Other x-ray optics with typically smaller apertures will have a greater value of normalized degree of coherence. The quality and reliability of both the probe and object functions can be visually evaluated using the reconstructed object shown in Fig. 3(a), where there is good agreement with known feature sizes from the fabrication design and scanning

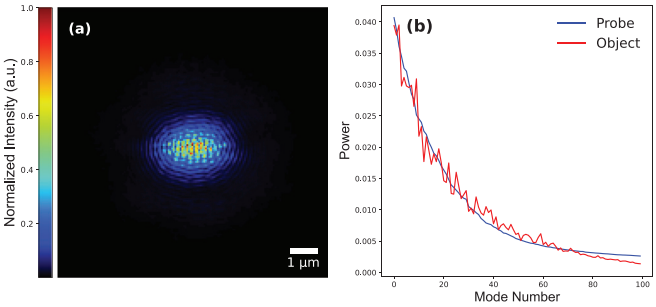

FIG. 2. (a) The normalized two-dimensional intensity of the multi-modal probe at the object position, found by summing the intensity contributions of the individual probe modes. (b) The power spectrum of the multi-modal probe modes after orthogonalization and the multi-modal object modes.

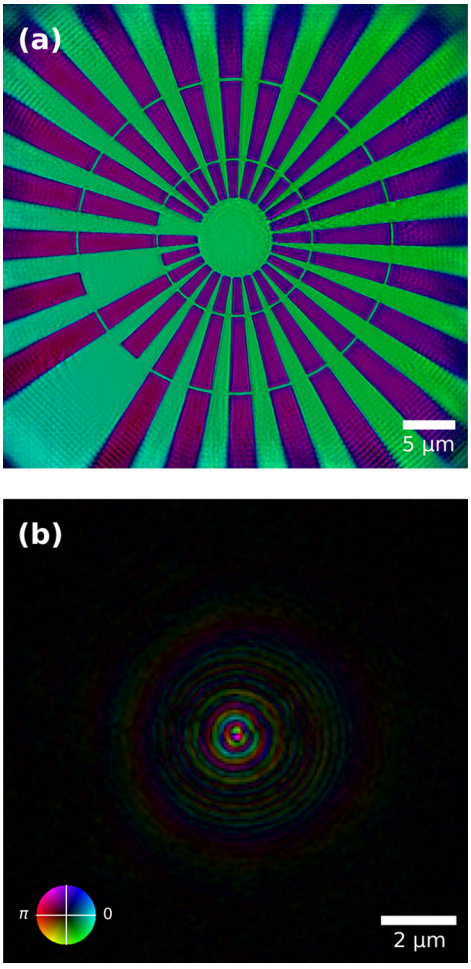

FIG. 3. Ptychographic reconstructions of the (a) Siemens star test object and (b) beryllium compound refractive lens illumination. The Siemens star test object in (a) is reconstructed using a multi-modal probe, while the probe in (b) is reconstructed using a multi-modal object. Both figures are complex plots, and the color wheel given in (b) is valid for both figures; brightness and hue represent the amplitude and phase, respectively.

© Author(s) 2021

electron microscope image included in the supplementary material. The spatial resolution of the reconstructions was sufficiently high to visually distinguish the 1 μm features separating the innermost radial spokes. To quantify the resolution further, Fourier shell correlation[14,34] was performed on two independent ptychography scans over the same object area and reconstructed with identical parameters. After alignment of the two reconstructions, the correlation between them was found to cross the 1/2-bit threshold with an estimated spatial resolution of 104 nm. The plot of this is also included in the supplementary material for completeness.

Since the ptychographic method recovers a complex wavefield for both the coherent and multi-modal probes, we are able to use the Fresnel–Kirchhoff diffraction formula to numerically propagate to any position along the optical axis. In order to compare the validity of the proposed method, we calculated the intensity of the coherent and multi-modal probes at various positions along the optical axis, including at the focus. This was achieved for the multi-modal probe by propagating each of the probe modes individually and calculating their contribution to the total intensity.[11] This is shown in Figs. 4(a) and 4(c), which demonstrate that the multi-modal probe is equivalent to the coherent probe convolved with a Gaussian, originating from the source contribution. The focal position was then defined as the plane, which maximized peak intensity and was found to be 2.3 mm upstream of the object for both coherent and multi-modal probes, as shown for the coherent probe in Fig. 4(b). The focal size of the multi-modal probe was found to be 1.22 μm (h) $\times$ 0.62 μm (v), which agrees well with previous knife-edge measurements and the effect of the demagnified source size on the focus. The focus profile of the coherent probe shown in Fig. 4(a) displays the prevalence of the optical aberrations more and also has a size much closer to the theoretical diffraction limited size. Additionally, when this focus is convolved with the Gaussian of the demagnified source contribution, it matches that of the multi-modal probe, similar to that is shown in Fig. 2(a).

The focal size and position obtained from the intensity at and around the focus provide only partial insight into the performance of an optic. To completely characterize the optical aberrations causing focal degradation, and design or introduce methods for correction,[35] requires the complete complex wavefield to be considered. The wavefront error is calculated from the path difference, which is directly related to the phase shift over the probe and given by

$$\Delta X = \frac{\lambda \Delta \varphi}{2\pi}, \tag{3}$$

where ΔX is the path difference, λ is the wavelength, and $\Delta\varphi$ is the phase shift. We first back propagated the coherent probe wavefield upstream of the object position by a distance of 432 mm + 2.3 mm to the exit plane of the Beryllium CRL array. The phase distribution was then unwrapped using the method presented in Ref. 36, which was found to be most effective at avoiding artifacts arising due to the presence of phase residues. From this, the phase of a perfect spherical wave[13] was fitted and subtracted with the Beryllium CRL design parameters according to

$$\Delta\varphi(x,y) = -k\left(\sqrt{\Delta z^2 + x^2 + y^2} - \Delta z\right), \tag{4}$$

where $\Delta\varphi$ is the phase, k is the wavenumber, and Δz is the ideal focal length. This was then converted to a path length (or wavefront) error

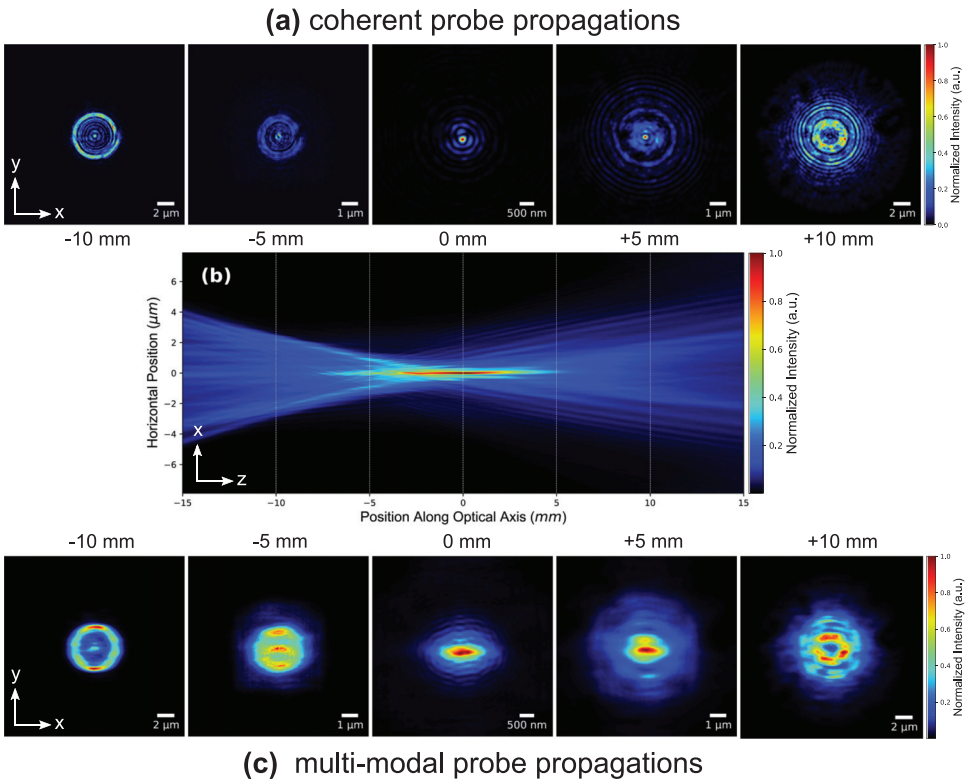

FIG. 4. Propagation of the reconstructed (a) coherent and (c) multi-modal probes to distances $\pm$10 mm about the focal position. (b) Summed intensity propagation along the optical axis of the coherent probe in the vicinity of the focal plane. The probes were propagated using the Fresnel–Kirchhoff equation, in the case of the multi-modal probe, the individual modes were propagated, and their contributions to the intensity were summed.

© Author(s) 2021

to compare with the data previously measured.[24] The previous measurement[24] used a knife-edge scanning technique working at an energy of 15 keV, and so to compare we assumed that the wavefront error occurs due to thickness variations in the lens array, which will change depending on the energy. Converting the wavefront error at one energy corresponds to a scaling factor given by the ratio of the real refractive index decrement at the two different energies,

$$\Delta X(E_1) = \Delta t\, \delta(E_1) = \frac{\delta(E_1)}{\delta(E_2)} \Delta X(E_2), \tag{5}$$

where $\Delta X(E)$ is the path length change, Δt is the aberration error thickness, $\delta(E)$ is the energy-dependent refractive index decrement for Beryllium, and the subscripts 1 and 2 denote the measurements at 15 and 12 keV, respectively. The results of this analysis are shown in Figs. 5(a) and 5(b) where we have also included the average radial profile calculated for the knife-edge measurement. The ptychographic profile demonstrates visually good agreement with the knife-edge results and even recovers the same asymmetry found around the 70 mm radial position. The root mean squared (RMS) wavefront error[24] was found to be 27.3 pm, which is also in good agreement with the 24.0 pm found using the knife-edge technique. While there is a slight difference in the RMS wavefront error and average radial profile, we believe this is because the knife edge is a one-dimension technique that was repeated at various polar angles and, thus, generated a fairly coarse two-dimensional grid of points for comparison. The ptychography measurement also demonstrates an advantage over the previous technique with its ability to recover the wavefront error over the complete aperture of the lens, whereas the knife-edge technique is sensitive to low intensity at the edges of the aperture.

Multi-modal ptychography has been used to recover both the coherent object (with multi-modal probe) and the coherent probe (with multi-modal object) in the presence of decoherence arising from a partially transverse-coherent source. From the coherent probe recovered during the ptychographic reconstruction, we were able to extract the wavefront error introduced by an aberrated Beryllium CRL and compare this with another experimentally validated technique. The relative power spectrum of the multi-modal probe estimates the proportion of coherent flux at 2%, significantly lower than that coherent diffraction imaging experiments typically use. Additionally, from the coherent object, we were able to demonstrate imaging of a Siemens star test object to spatial resolutions of 104 nm, which is much smaller than the 500 nm typically offered by the beamline. The procedure for characterizing optical aberrations presented in this Letter is expected to valid for a wide variety of x-ray optics including refractive optics (as demonstrated), diffractive optics such as Fresnel zone plates and multilayer Laue lenses, and reflective mirror optics. Our results demonstrate the ability of multi-modal ptychography to reconstruct using relatively low levels of transverse-coherence and also pave the way for synchrotron facilities to offer high-resolution, nanoscale imaging and optics characterization regardless of the source characteristics.

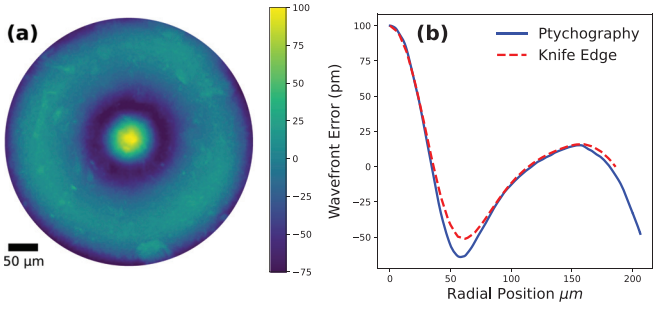

FIG. 5. The (a) two-dimensional and (b) radially averaged wavefront error for the beryllium compound refractive lens at 15 keV. The ptychographic results were converted to the 15 keV wavefront error for comparison with previous measurements using a knife-edge technique.

See the supplementary material for additional figures and information recovered during the ptychographic reconstruction process and the Fourier ring correlation analysis.

This work was carried out with the support of the Diamond Light Source. The authors thank Andrew Malandain for technical support during the measurements on the B16 Test beamline. We thank Benedikt Daurer and Arron Parson for their assistance with initial use and implementation of the ptypy Python package. We would also like to acknowledge the use of the High Performance Cluster computing facilities at the Diamond Light Source.

DATA AVAILABILITY

The raw and processed datasets that support the findings of this study are openly available in the Zenodo public repository and can be accessed at https://doi.org/10.5281/zenodo.4468745.

REFERENCES

[1]J. Miao, P. Charalambous, J. Kirz, and D. Sayre, "Extending the methodology of x-ray crystallography to allow imaging of micrometre-sized non-crystalline specimens," Nature **400**, 342–344 (1999).
[2]J. M. Rodenburg, A. C. Hurst, A. G. Cullis, B. R. Dobson, F. Pfeiffer, O. Bunk, C. David, K. Jefimovs, and I. Johnson, "Hard-x-ray lensless imaging of extended objects," Phys. Rev. Lett. **98**, 034801 (2007).
[3]P. Thibault, M. Dierolf, A. Menzel, O. Bunk, C. David, and F. Pfeiffer, "High-resolution scanning x-ray diffraction microscopy," Science **321**, 379–382 (2008).
[4]Z. Chen, M. Odstrcil, Y. Jiang, Y. Han, M.-H. Chiu, L.-J. Li, and D. A. Muller, "Mixed-state electron ptychography enables sub-angstrom resolution imaging with picometer precision at low dose," Nat. Commun. **11**, 2994 (2020).
[5]N. Anthony, C. Darmanin, M. R. Bleackley, K. Parisi, G. Cadenazzi, S. Holmes, M. A. Anderson, K. A. Nugent, and B. Abbey, "Ptychographic imaging of nad1 induced yeast cell death," Biomed. Opt. Express **10**, 4964–4974 (2019).
[6]C. Donnelly, V. Scagnoli, M. Guizar-Sicairos, M. Holler, F. Wilhelm, F. Guillou, A. Rogalev, C. Detlefs, A. Menzel, J. Raabe, and L. J. Heyderman, "High-resolution hard x-ray magnetic imaging with dichroic ptychography," Phys. Rev. B **94**, 064421 (2016).
[7]M. Dierolf, A. Menzel, P. Thibault, P. Schneider, C. M. Kewish, R. Wepf, O. Bunk, and F. Pfeiffer, "Ptychographic x-ray computed tomography at the nanoscale," Nature **467**, 436–439 (2010).
[8]P. Li and A. Maiden, "Multi-slice ptychographic tomography," Sci. Rep. **8**, 2049 (2018).
[9]L. R. Brandt, J.-J. Marie, T. Moxham, D. P. Förstermann, E. Salvati, C. Besnard, C. Papadaki, Z. Wang, P. G. Bruce, and A. M. Korsunsky, "Synchrotron x-ray quantitative evaluation of transient deformation and damage phenomena in a single nickel-rich cathode particle," Energy Environ. Sci. **13**, 3556–3566 (2020).
[10]K. Sawhney, H. Wang, J. Sutter, S. Alcock, and S. Berujon, "At-wavelength metrology of x-ray optics at diamond light source," Synchrotron Radiat. News **26**, 17–22 (2013).

© Author(s) 2021

[11]T. E. J. Moxham, A. Parsons, T. Zhou, L. Alianelli, H. Wang, D. Laundy, V. Dhamgaye, O. J. L. Fox, K. Sawhney, and A. M. Korsunsky, "Hard X-ray ptychography for optics characterization using a partially coherent synchrotron source," J. Synchrotron Radiat. **27**, 1688–1695 (2020).
[12]C. M. Kewish, M. Guizar-Sicairos, C. Liu, J. Qian, B. Shi, C. Benson, A. M. Khounsary, J. Vila-Comamala, O. Bunk, J. R. Fienup, A. T. Macrander, and L. Assoufid, "Reconstruction of an astigmatic hard x-ray beam and alignment of K-B mirrors from ptychographic coherent diffraction data," Opt. Express **18**, 23420–23427 (2010).
[13]F. Seiboth, A. Schropp, M. Scholz, F. Wittwer, C. Rödel, M. Wünsche, T. Ullsperger, S. Nolte, J. Rahomäki, K. Parfeniukas, S. Giakoumidis, U. Vogt, U. Wagner, C. Rau, U. Boesenberg, J. Garrevoet, G. Falkenberg, E. C. Galtier, H. Ja Lee, B. Nagler, and C. G. Schroer, "Perfect x-ray focusing via fitting corrective glasses to aberrated optics," Nat. Commun. **8**, 14623 (2017).
[14]J. Vila-Comamala, A. Diaz, M. Guizar-Sicairos, A. Mantion, C. M. Kewish, A. Menzel, O. Bunk, and C. David, "Characterization of high-resolution diffractive x-ray optics by ptychographic coherent diffractive imaging," Opt. Express **19**, 21333–21344 (2011).
[15]X. Huang, M. Wojcik, N. Burdet, I. Peterson, G. R. Morrison, D. J. Vine, D. Legnini, R. Harder, Y. S. Chu, and I. K. Robinson, "Quantitative x-ray wavefront measurements of Fresnel zone plate and K-B mirrors using phase retrieval," Opt. Express **20**, 24038–24048 (2012).
[16]A. Schropp, R. Hoppe, V. Meier, J. Patommel, F. Seiboth, H. J. Lee, B. Nagler, E. C. Galtier, B. Arnold, U. Zastrau, J. B. Hastings, D. Nilsson, F. Uhlén, U. Vogt, H. M. Hertz, and C. G. Schroer, "Full spatial characterization of a nanofocused x-ray free-electron laser beam by ptychographic imaging," Sci. Rep. **3**, 1633 (2013).
[17]S. Sala, B. J. Daurer, M. Odstrcil, F. Capotondi, E. Pedersoli, M. F. Hantke, M. Manfredda, N. D. Loh, P. Thibault, and F. R. N. C. Maia, "Pulse-to-pulse wavefront sensing at free-electron lasers using ptychography," J. Appl. Crystallogr. **53**, 949–956 (2020).
[18]L. W. Whitehead, G. J. Williams, H. M. Quiney, D. J. Vine, R. A. Dilanian, S. Flewett, K. A. Nugent, A. G. Peele, E. Balaur, and I. McNulty, "Diffractive imaging using partially coherent x rays," Phys. Rev. Lett. **103**, 243902 (2009).
[19]P. Thibault and A. Menzel, "Reconstructing state mixtures from diffraction measurements," Nature **494**, 68–71 (2013).
[20]J. C. da Silva, A. Pacureanu, Y. Yang, S. Bohic, C. Morawe, R. Barrett, and P. Cloetens, "Efficient concentration of high-energy x-rays for diffraction-limited imaging resolution," Optica **4**, 492–495 (2017).
[21]H. Öztürk, H. Yan, Y. He, M. Ge, Z. Dong, M. Lin, E. Nazaretski, I. K. Robinson, Y. S. Chu, and X. Huang, "Multi-slice ptychography with large numerical aperture multilayer laue lenses," Optica **5**, 601–607 (2018).
[22]P. M. Pelz, M. Guizar-Sicairos, P. Thibault, I. Johnson, M. Holler, and A. Menzel, "On-the-fly scans for x-ray ptychography," Appl. Phys. Lett. **105**, 251101 (2014).
[23]J. N. Clark, X. Huang, R. J. Harder, and I. K. Robinson, "Dynamic imaging using ptychography," Phys. Rev. Lett. **112**, 113901 (2014).
[24]V. Dhamgaye, D. Laundy, S. Baldock, T. Moxham, and K. Sawhney, "Correction of the X-ray wavefront from compound refractive lenses using 3D printed refractive structures," J. Synchrotron Radiat. **27**, 1518–1527 (2020).
[25]B. Enders, M. Dierolf, P. Cloetens, M. Stockmar, F. Pfeiffer, and P. Thibault, "Ptychography with broad-bandwidth radiation," Appl. Phys. Lett. **104**, 171104 (2014).
[26]K. J. S. Sawhney, I. P. Dolbnya, M. K. Tiwari, L. Alianelli, S. M. Scott, G. M. Preece, U. K. Pedersen, and R. D. Walton, "A test beamline on diamond light source," AIP Conf. Proc. **1234**, 387–390 (2010).
[27]T. B. Edo, D. J. Batey, A. M. Maiden, C. Rau, U. Wagner, Z. D. Pešić, T. A. Waigh, and J. M. Rodenburg, "Sampling in x-ray ptychography," Phys. Rev. A **87**, 053850 (2013).
[28]J. C. da Silva and A. Menzel, "Elementary signals in ptychography," Opt. Express **23**, 33812–33821 (2015).
[29]B. Enders and P. Thibault, "A computational framework for ptychographic reconstructions," Proc. R. Soc. A **472**, 20160640 (2016).
[30]P. Thibault, M. Dierolf, O. Bunk, A. Menzel, and F. Pfeiffer, "Probe retrieval in ptychographic coherent diffractive imaging," Ultramicroscopy **109**, 338–343 (2009).
[31]A. Maiden, D. Johnson, and P. Li, "Further improvements to the ptychographical iterative engine," Optica **4**, 736–745 (2017).
[32]R. Okuta, Y. Unno, D. Nishino, S. Hido, and C. Loomis, "Cupy a numpy-compatible library for NVIDIA GPU calculations," in Proceedings of Workshop on Machine Learning Systems (LearningSys) in the Thirty-First Annual Conference on Neural Information Processing Systems (NIPS) (2017).
[33]F. van der Veen and F. Pfeiffer, "Coherent x-ray scattering," J. Phys. **16**, 5003–5030 (2004).
[34]M. van Heel and M. Schatz, "Fourier shell correlation threshold criteria," J. Struct. Biol. **151**, 250–262 (2005).
[35]D. Laundy, V. Dhamgaye, T. Moxham, and K. Sawhney, "Adaptable refractive correctors for x-ray optics," Optica **6**, 1484–1490 (2019).
[36]H. Xia, S. Montresor, R. Guo, J. Li, F. Yan, H. Cheng, and P. Picart, "Phase calibration unwrapping algorithm for phase data corrupted by strong decorrelation speckle noise," Opt. Express **24**, 28713–28730 (2016).

© Author(s) 2021